Nuclear Science and Techniques (2026) 37:108
https://doi.org/10.1007/s41365-026-01941-2

# Online beam phase calibration with detuning compensation for normal-conducting cavities under closed-loop operation

Feng Qiu[1,2] · Cheng-Ye Xu[1] · Ri-Hua Zeng[3] · Yuan He[1,2] · Shi-Hui Wei[1] · Jia-Yi Peng[1,2] · Li-Juan Yang[1] · Zi-Qin Yang[1] · Zhou-Li Zhang[1] · Zhi-Jun Wang[1] · Mu-Yuan Wang[4] · Cecilia Maiano[4] · Paolo Pierini[4]

Received: 2 May 2025 / Revised: 7 June 2025 / Accepted: 11 July 2025 / Published online: 27 March 2026


**Abstract**
Accurate calibration of the beam phase (i.e., the phase of the beam arrival relative to the cavity accelerating field) is essential for maintaining the stability and efficiency of linear accelerators. Conventional offline phase-scan methods, such as the $\Delta T$ phase scan and phase-scan signature matching, are typically performed during commissioning or maintenance, requiring the accelerator to be taken out of normal operation. Moreover, these methods cannot effectively track the gradual drifts caused by ambient conditions. An online beam phase calibration technique using beam-induced radio-frequency (RF) transients was initially developed at DESY for superconducting cavities operating under open-loop conditions. Extending the DESY method to normal-conducting cavities at the European Spallation Source (ESS) introduces challenges. When the beam pulse length approaches the cavity time constant $\tau = 1/\omega_{0.5}$, where $\omega_{0.5}$ is the cavity half bandwidth, the detuning effects distort the trajectory of the beam-induced RF transient and degrade the beam phase measurement accuracy. Furthermore, open-loop operation is generally not advisable for high-current proton linacs because of stability and safety concerns associated with the operation. To address these issues, we revisited the cavity differential equations and proposed a detuning compensation method that corrects the distorted trajectory in the in-phase/quadrature plane of the laser beam. In addition, by analyzing the initial 1.4 $\mu$s transient response before low-level RF (LLRF) feedback becomes active, beam phase calibration can be achieved under closed-loop operation. The experimental results indicate that the proposed method agrees well with beam position monitor (BPM)-based measurements. This approach enables real-time beam phase monitoring without interrupting the closed-loop operation and can be adapted to similar accelerator systems.

**Keywords** Beam phase calibration · Transient beam loading · Detuning effect · Closed-loop operation · Low-level RF systems · Normal-conducting cavity · Particle accelerator

This work was supported by the studies of intelligent LLRF control algorithms for superconducting RF cavities (No. E129851YR0), the National Natural Science Foundation of China (No. U22A20261), and R&D of Intelligent Technologies for Next-Generation Industrial Linear Accelerators (HNN25XMMXWL).

✉ Feng Qiu
qiufeng@impcas.ac.cn

✉ Yuan He
hey@impcas.ac.cn

1 Institute of Modern Physics, Chinese Academy of Sciences, Lanzhou 730000, China

2 School of Nuclear Science and Technology, University of Chinese Academy of Sciences, Beijing 100049, China

3 Advanced Energy Science and Technology Guangdong Laboratory, Huizhou 516000, China

4 European Spallation Source ERIC, 22100 Lund, Sweden

## 1 Introduction

The European Spallation Source (ESS) in Lund, Sweden, is constructing a high-intensity 2 GeV proton linear accelerator designed for 5 MW operation [1]. The accelerator comprises a normal-conducting (NC) front end operating at 352.21 MHz, followed by a superconducting (SC) linac at 704.42 MHz (excluding the spoke cavities). As shown in Fig. 1, the drift tube linac (DTL) and SC sections are subdivided into individual tanks and cryomodules, with the gray-shaded cryomodules designated to remain unpowered during the initial 2 MW operation at 800 MeV [2–4]. The high-level parameters for the ESS are summarized in Table 1. Designed for a 62.5 mA peak beam current with a 14 Hz repetition rate, the ESS demands accurate and precise

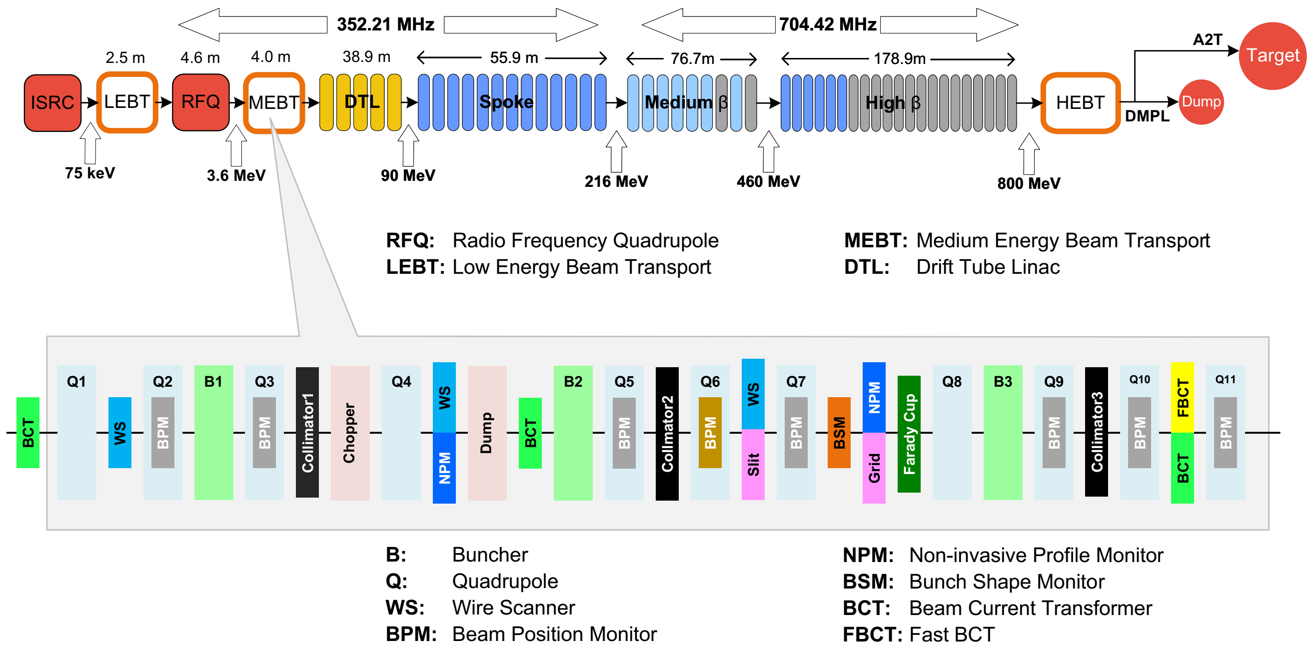


**Fig. 1** (Color online) Schematic layout of the ESS linac operations at 800 MeV and 2 MW (upper plot) and a detailed view of the MEBT section (lower plot) [2]. In the upper plot, each segment in the drift tube linac (DTL) and SC sections represents a DTL tank or a cryomodule, with the gray-shaded cryomodules indicating those that will remain unpowered during the initial 2 MW operation at 800 MeV. The lower plot provides an expanded view of the MEBT section, detailing its beam matching optics and diagnostic components essential for shaping and monitoring the beam. Three buncher cavities, labeled B1 to B3, are installed within the MEBT to maintain the longitudinal focus of the beam

**Table 1** ESS linac high-level parameters [2]

| Parameter | Value |
|---|---|
| Beam power (MW) | 5 |
| Beam energy (GeV) | 2 |
| Peak beam current (mA) | 62.5 |
| Beam pulse length (ms) | 2.86 |
| Beam pulse repetition rate (Hz) | 14 |
| Duty factor (%) | 4 |
| RF frequency (MHz) | 352.21 / 704.42 |
| Availability (%) | 95 |

RF phase control in each cavity to maintain beam quality and minimize beam losses. By 2023, the initial commissioning had accelerated the beam through the early NC sections to approximately 74 MeV.

Accurate measurement of the beam phase, defined as the phase experienced by the beam relative to the RF field, is critical for maintaining beam quality and minimizing losses, particularly in high-power accelerators such as the ESS. Various methods exist for calibrating beam phases. Direct approaches include phase-scan techniques (e.g., $\Delta T$ phase scan [4–7], phase-scan signature matching [7, 8]), which vary the RF phase and observe downstream beam changes. Although effective, these methods often need dedicated beam studies, requiring the sequential calibration of individual cavities with adjacent ones deactivated or significantly detuned, thereby disrupting normal operations. They are typically performed offline during commissioning or maintenance, making them labor-intensive. Furthermore, gradual ambient drifts, such as changes in temperature and humidity, within low-level RF (LLRF) control loops necessitate periodic recalibrations during routine operation.

Alternative strategies have been designed to minimize the disruption of the normal operation of the accelerator. The "drifting beam method", pioneered at SNS [9], uses the LLRF system to measure transient RF signals excited by the beam in an unpowered SC cavity. The analysis of these transients yields the relative beam phase. This avoids extra beam diagnostics but requires temporarily unpowering the cavity. Researchers at DESY proposed another method based on the linear fitting of the trajectory of the RF transient induced by a beam pulse in the in-phase/quadrature (I/Q) plane. The beam pulse is typically short, on the order of tens of microseconds, and the measurement is performed within a powered SC cavity [10–14]. The DESY approach allows online measurement but usually requires operating the SC cavity in an open-loop configuration.

Adapting the DESY approach to the ESS NC buncher cavity poses a distinct challenge [15, 16]. The buncher cavity has a measured half-bandwidth ($\omega_{0.5}$) of approximately 18 kHz, corresponding to a time constant ($\tau = \frac{1}{\omega_{0.5}}$) of about 9 µs. When using short diagnostic beam pulses (e.g., 5 µs) whose duration is comparable to $\tau$, cavity detuning causes a significant nonlinear rotation (deflection) of the beam-induced RF transient trajectory. Consequently, the trajectory deviates from the expected linear behavior, which substantially reduces the accuracy of the beam phase calibration based on linear fitting. This issue is less pronounced in SRF cavities, where the time constants are typically on the order of milliseconds owing to their much higher loaded quality factors ($Q_L$) [17–21].

To mitigate detuning-induced errors, we developed a detuning compensation algorithm by solving the cavity differential equations to predict the theoretical deflection angle ($\alpha_{th}$) of the transient trajectory. Subtracting the calculated $\alpha_{th}$ from the fitted angle from the RF transient trajectory enables accurate beam phase calibration.

However, operating RF cavities in the open-loop mode is neither practical nor safe for high-current proton linacs, such as the ESS. In open-loop operation, the RF field can deviate from its setpoint, and strong beam loading [22, 23] further increases the risk of beam losses. Therefore, it is preferable to maintain a closed-loop LLRF operation during measurements. To avoid interference from the feedback system during phase calibration, we deliberately selected a calibration window approximately equal to the LLRF loop delay ($\tau_d \approx 1.4$ µs) and restricted the analysis to the beam-induced RF transient before the feedback loop became active. This ensures that only the portion of the transient signal unaffected by the feedback is considered, allowing beam phase calibration under closed-loop conditions. It should be noted that the closed-loop measurement relies solely on the first 1.4 µs of transient data to determine the beam phase. Although the achievable phase precision is inherently limited compared to open-loop or BPM-based methods, this approach enables online phase monitoring under normal operating conditions of the device. The resulting $\pm 2.5°$ accuracy is generally considered adequate for routine diagnostics, machine protection, and early fault detection [23].

In the following sections, we first revisit the cavity differential equation and analyze the impact of cavity detuning on the beam-induced RF transient. Based on this analysis, a detuning-aware beam phase calibration method is proposed, together with a practical implementation strategy under closed-loop conditions. Experimental validation was performed using the ESS MEBT buncher cavity, demonstrating the effectiveness of the proposed technique under realistic operating scenarios.

## 2 Principle of beam phase calibration using beam-induced RF transients

The beam phase calibration method based on beam-induced RF transients in powered RF cavities was originally proposed by DESY [13, 14]. In the following subsection, we present the theoretical basis of DESY's approach, including the derivation of the transient field trajectory and the conditions under which the linear approximation applies directly. Throughout this study, boldface symbols (e.g., $\mathbf{V}_c$, $\mathbf{I}_b$) denote complex-valued signals or quantities.

### 2.1 Transient RF trajectory calibration: concept and example

Figure 2 illustrates the basic principle of beam phase measurement using beam-induced RF transients. As shown in Fig. 2a, the cavity field is initially in a steady state with normalized amplitude and zero phase. When a short beam pulse passes through the cavity in the open-loop mode, it induces a transient perturbation, denoted as $\mathbf{V}_{cb}(t)$, shifting the cavity voltage from its nominal value to a new complex value $A_{tail}e^{j\theta_{tail}}$. This transient response traces a trajectory in the I/Q plane (Fig. 2b), where the horizontal axis represents the in-phase (I, real) component, and the vertical axis represents the quadrature (Q, imaginary) component. The angle $\varphi_b$ between the steady-state $\mathbf{V}_c$ vector and the direction of this trajectory reflects the beam phase [11, 13, 14, 24, 25].

Figure 3 shows the measured beam-induced RF transient in the ESS buncher cavity B2 (see Fig. 1) under open-loop conditions, generated by a 5 µs, 55 mA beam pulse with a beam phase of approximately −44°. The relevant RF parameters are listed in Table 2. As seen in Fig. 3a,

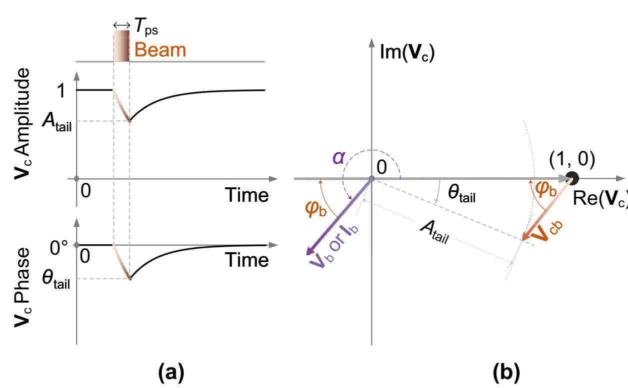


**Fig. 2** Principle of beam phase measurement using beam-induced RF transient response, as proposed by DESY. **a** Time-domain evolution of the cavity voltage amplitude and phase for the transient signal $\mathbf{V}_{cb}(t)$ when a short beam pulse traverses an RF cavity in the open-loop mode. **b** Corresponding trajectory of $\mathbf{V}_{cb}(t)$ in the I/Q plane, where the direction of the trajectory reflects the beam phase

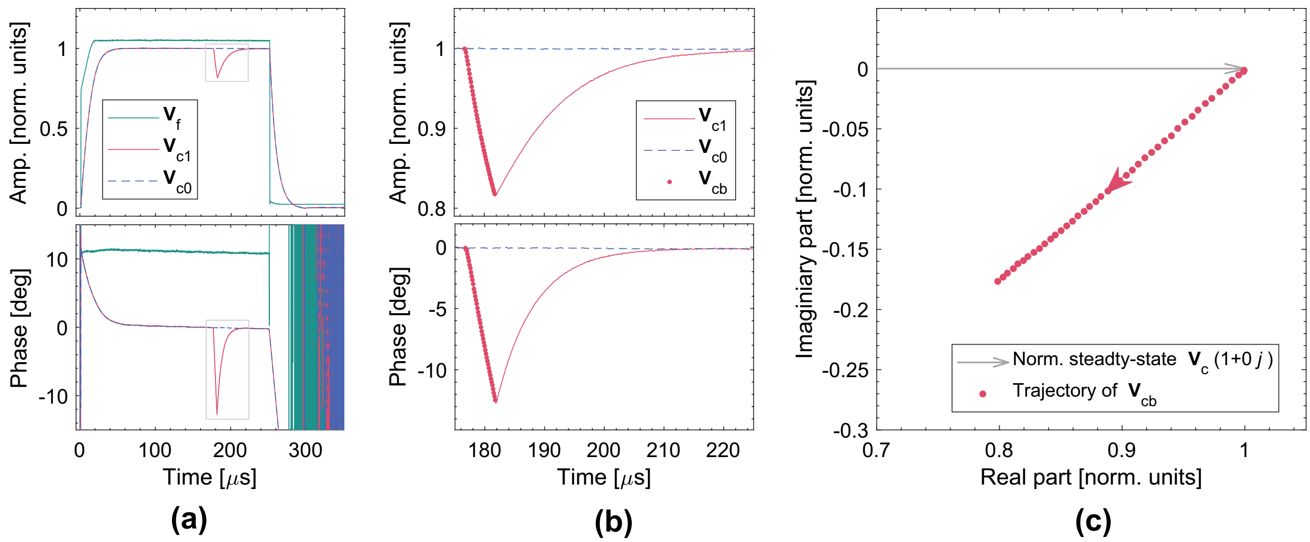


**Fig. 3** (Color online) Measured beam-induced RF transient in the ESS buncher cavity B2 under open-loop conditions with a 5 μs and 55 mA beam pulse. **a** Time evolution of the forward voltage $\mathbf{V}_\mathrm{f}$, cavity voltage with beam $\mathbf{V}_\mathrm{c1}$, and cavity voltage without beam $\mathbf{V}_\mathrm{c0}$. **b** Zoomed-in view of the beam-induced RF transient in both the amplitude and phase. The red dots represent the sampled values of $\mathbf{V}_\mathrm{cb}$ recorded by the LLRF DAQ system, with a sampling period of approximately 0.119 μs. **c** Trajectory of the beam-induced transient vector $V_\mathrm{cb}$ in I/Q plane. Due to a detuning angle of approximately $-11°$ in the cavity, the trajectory is slightly deflected toward the negative direction of the $X$-axis (real axis)

**Table 2** RF parameters for ESS buncher cavity B2 (see Fig. 1)

| Parameter | Value |
|---|---|
| Beam pulse repetition rate (Hz) | 14 |
| Cavity voltage (kV) | 59.7 |
| RF frequency (MHz) | 352.21 |
| Cavity half bandwidth ($\omega_{0.5}$) (kHz) | ~18 |
| Normalized shunt impedance ($r/Q$) (Ω) | ~75 |
| Coupling factor ($\beta$) | ~1 |

the cavity remains in a steady state prior to beam arrival. At approximately $t = 177$ μs, the cavity voltage $\mathbf{V}_\mathrm{c1}(t)$ in the presence of the beam exhibits a pronounced drop in both the amplitude and phase relative to the no-beam case $\mathbf{V}_\mathrm{c0}(t)$. A zoomed-in view of the shaded region in Fig. 3a, as shown in Fig. 3b reveals the detailed structure of the beam-induced RF transient. Figure 3c displays the corresponding transient trajectory of $\mathbf{V}_\mathrm{cb}(t)$ in the I/Q plane, reconstructed from the sampled RF waveforms acquired by the digital LLRF system.

In the following, we present the theoretical basis of this approach, including the derivation of the transient field expression and the conditions under which the linear approximation remains valid.

The time evolution of the cavity field, with and without beam loading, can be described by the following differential equations [24, 26–30]:

$$\begin{cases} \mathbf{V}'_\mathrm{c0}(t) + (\omega_{0.5} - j\Delta\omega_0)\mathbf{V}_\mathrm{c0}(t) = \dfrac{2\beta\omega_{0.5}}{1+\beta}\mathbf{V}_\mathrm{f0}(t) \\ \mathbf{V}'_\mathrm{c1}(t) + (\omega_{0.5} - j\Delta\omega_1)\mathbf{V}_\mathrm{c1}(t) = \dfrac{2\beta\omega_{0.5}}{1+\beta}\mathbf{V}_\mathrm{f1}(t) + \omega_{0.5}\mathbf{V}_\mathrm{b}(t) \end{cases} \tag{1}$$

In these equations, $t$ denotes the time. The variables $\mathbf{V}_\mathrm{f0}$ and $\mathbf{V}_\mathrm{f1}$ denote the cavity forward voltages without and with the beam, respectively. The detuning terms $\Delta\omega_0$ and $\Delta\omega_1$ account for the cavity detuning in the absence and presence of the beam, respectively. The parameter $\omega_{0.5}$ is the cavity half-bandwidth, assumed to be independent of beam loading, and $\beta$ is the coupling coefficient of the input coupler. The beam-induced voltage $\mathbf{V}_\mathrm{b}(t)$ is given by

$$\mathbf{V}_\mathrm{b}(t) = R_\mathrm{L}\mathbf{I}_\mathrm{b}(t), \tag{2}$$

where $\mathbf{I}_\mathrm{b}(t)$ is the RF component of the bunched beam current. The commonly referenced beam current typically refers to its average (DC) value. For short bunches, the RF current amplitude satisfies $|\mathbf{I}_\mathrm{b}| \approx 2I_\mathrm{b0}$, where $I_\mathrm{b0}$ is the DC beam current [26]. The loaded resistance $R_\mathrm{L}$ is defined as

$$R_\mathrm{L} = 0.5\left(\frac{r}{Q}\right)Q_\mathrm{L}, \tag{3}$$

where $Q_\mathrm{L}$ is the loaded quality factor of the cavity and $r/Q$ is the normalized shunt impedance.

If the cavity operates in an open-loop mode, the cavity forward signal remains approximately unchanged during beam injection, such that $\mathbf{V}_{\mathrm{f0}}(t) \approx \mathbf{V}_{\mathrm{f1}}(t)$. We also assume that the cavity detuning is approximately constant throughout the beam pulse. Accordingly, we set $\Delta\omega_0 \approx \Delta\omega_1 \equiv \Delta\omega$. Under these assumptions, subtracting the first equation in Eq. (1) from the second yields:

$$\frac{\mathrm{d}\mathbf{V}_{\mathrm{cb}}(t)}{\mathrm{d}t} + (\omega_{0.5} - j\Delta\omega)\mathbf{V}_{\mathrm{cb}}(t) = \omega_{0.5}\mathbf{V}_{\mathrm{b}}(t). \tag{4}$$

The general solution of Eq. (4) for zero initial condition (i.e., the zero-state response) is given by:

$$\mathbf{V}_{\mathrm{cb}}(t) = \omega_{0.5}\int_0^t e^{-\lambda(t-x)}\mathbf{V}_{\mathrm{b}}(x)\,\mathrm{d}x, \quad \text{for } t \geq 0, \tag{5}$$

where $\lambda = \omega_{0.5} - j\Delta\omega$.

To simplify the analysis without loss of generality, we assume that the beam-induced voltage $\mathbf{V}_{\mathrm{b}}(t)$ points along the $X$-axis (real axis) in the complex plane; that is, its phase angle is set to zero. Under this assumption, $\mathbf{V}_{\mathrm{b}}(t) \in \mathbb{R}^+$. For analytical convenience, we further model the beam input as a unit step function: $\mathbf{V}_{\mathrm{b}}(t) = u(t)$, where $u(t) = 0$ for $t < 0$ and $u(t) = 1$ for $t \geq 0$.

This approximation is justified by the fact that, as shown in Sect. 4, the beam current pulse typically resembles a quasi-rectangular waveform with a submicrosecond rise time. Hence, in the early stage, when the beam first enters the cavity, its effect closely resembles that of a step excitation. With this simplification, the solution to Eq. (4) becomes [27]:

$$\mathbf{V}_{\mathrm{cb,\,step}}(t) = \frac{\omega_{0.5}}{\omega_{0.5} - j\Delta\omega}\left[1 - e^{-(\omega_{0.5} - j\Delta\omega)t}\right], \quad \text{for } t > 0. \tag{6}$$

If the cavity is operated exactly on-resonance (i.e., $\Delta\omega$=0), Eq. (6) simplifies to

$$\mathbf{V}_{\mathrm{cb,\,step}}(t) = 1 - e^{-\omega_{0.5}t}. \tag{7}$$

In this ideal case, the exponential term remains purely real, and both $\mathbf{V}_{\mathrm{cb,step}}(t)$ and $\mathbf{V}_{\mathrm{b}}(t)$ lie along the $X$-axis in the I/Q plane. Consequently, the trajectory of $\mathbf{V}_{\mathrm{cb,step}}(t)$ remains aligned with $\mathbf{V}_{\mathrm{b}}(t)$, leading to no phase distortion.

## 2.2 Detuning impact analysis

When the cavity operates off-resonance ($\Delta\omega \neq 0$), the solution $\mathbf{V}_{\mathrm{cb,step}}(t)$ in Eq. (6) becomes complex, containing both real and imaginary components. Consequently, its trajectory deviates from the direction of $\mathbf{V}_{\mathrm{b}}$, undergoing a rotation in the I/Q plane. The direction of this rotation, clockwise or counterclockwise, depends on the sign of the detuning.

To gain analytical insight into the early-time behavior, we consider the limit $t \ll \tau$, where $\tau = 1/\omega_{0.5}$ denotes the cavity time constant. We further assume that $|\Delta\omega| \leq \omega_{0.5}$, which is typically satisfied by most RF cavities. Under this assumption, the product $(\omega_{0.5} - j\Delta\omega)t$ remains small, allowing the exponential term to be approximated using a second-order Taylor expansion as follows:

$$e^{-(\omega_{0.5} - j\Delta\omega)t} \approx 1 - (\omega_{0.5} - j\Delta\omega)t + \frac{(\omega_{0.5} - j\Delta\omega)^2 t^2}{2}.$$

Substituting this approximation into Eq. (6), we get:

$$\mathbf{V}_{\mathrm{cb,step}}(t) \approx \omega_{0.5}t - \frac{\omega_{0.5}(\omega_{0.5} - j\Delta\omega)t^2}{2},$$

which can be separated into real and imaginary parts:

$$\begin{cases} \Re[\mathbf{V}_{\mathrm{cb,step}}(t)] \approx \omega_{0.5}\,t - \dfrac{(\omega_{0.5}t)^2}{2}, \\ \Im[\mathbf{V}_{\mathrm{cb,step}}(t)] \approx \dfrac{\omega_{0.5}\,\Delta\omega\,t^2}{2}, \end{cases} \quad \text{for } t \to 0^+. \tag{8}$$

Accordingly, the ratio between the imaginary and real components is

$$\frac{\Im[\mathbf{V}_{\mathrm{cb,step}}(t)]}{\Re[\mathbf{V}_{\mathrm{cb,step}}(t)]} \approx \frac{\frac{1}{2}\Delta\omega\,t}{1 - \frac{1}{2}\omega_{0.5}t} \approx \frac{1}{2}\Delta\omega\,t, \quad \text{for } t \to 0^+. \tag{9}$$

According to Eq. (9), as $t \to 0^+$, the ratio between the imaginary and real components approaches zero, indicating that the imaginary part becomes negligible compared with the real part. Consequently, $\mathbf{V}_{\mathrm{cb,step}}(t)$ remains nearly aligned with the direction of $\mathbf{V}_{\mathrm{b}}$, which is assumed to lie along the $X$-axis.

Figure 4 shows $\mathbf{V}_{\mathrm{cb,step}}(t)$ under various detuning conditions. In Fig. 4a, both real and imaginary components evolve over time, with the response angle determined by the detuning angle $\Delta\theta = \tan^{-1}(\Delta\omega/\omega_{0.5})$. The early-time behavior ($t < 0.5\tau$) is shown in Fig. 4b, where the imaginary component remains small. The I/Q trajectories in Fig. 4c illustrate that detuning causes the response to deviate from the direction of $\mathbf{V}_{\mathrm{b}}$, which is assumed to lie along the X-axis. For negative detuning, the real part remains unchanged, whereas the imaginary part reverses sign, resulting in symmetry about the X-axis (not shown). As shown in Fig. 4d, the very initial trajectory ($t < 0.02\tau$) remains nearly aligned with the $X$-axis even for detuning angles up to 40°, which is consistent with Eq. (9). According to this expression, as $t \to 0^+$, the imaginary-to-real ratio approaches zero, indicating that $\mathbf{V}_{\mathrm{cb,step}}(t)$ initially aligns with the direction of $\mathbf{V}_{\mathrm{b}}$. This confirms that for $t \ll \tau$, the detuning-induced phase distortion is typically negligible.

Figure 4 and Eq. (8) provide insight into the applicability of the DESY method. When cavity detuning is present, the step response $\mathbf{V}_{\mathrm{cb,step}}(t)$ includes an imaginary component,

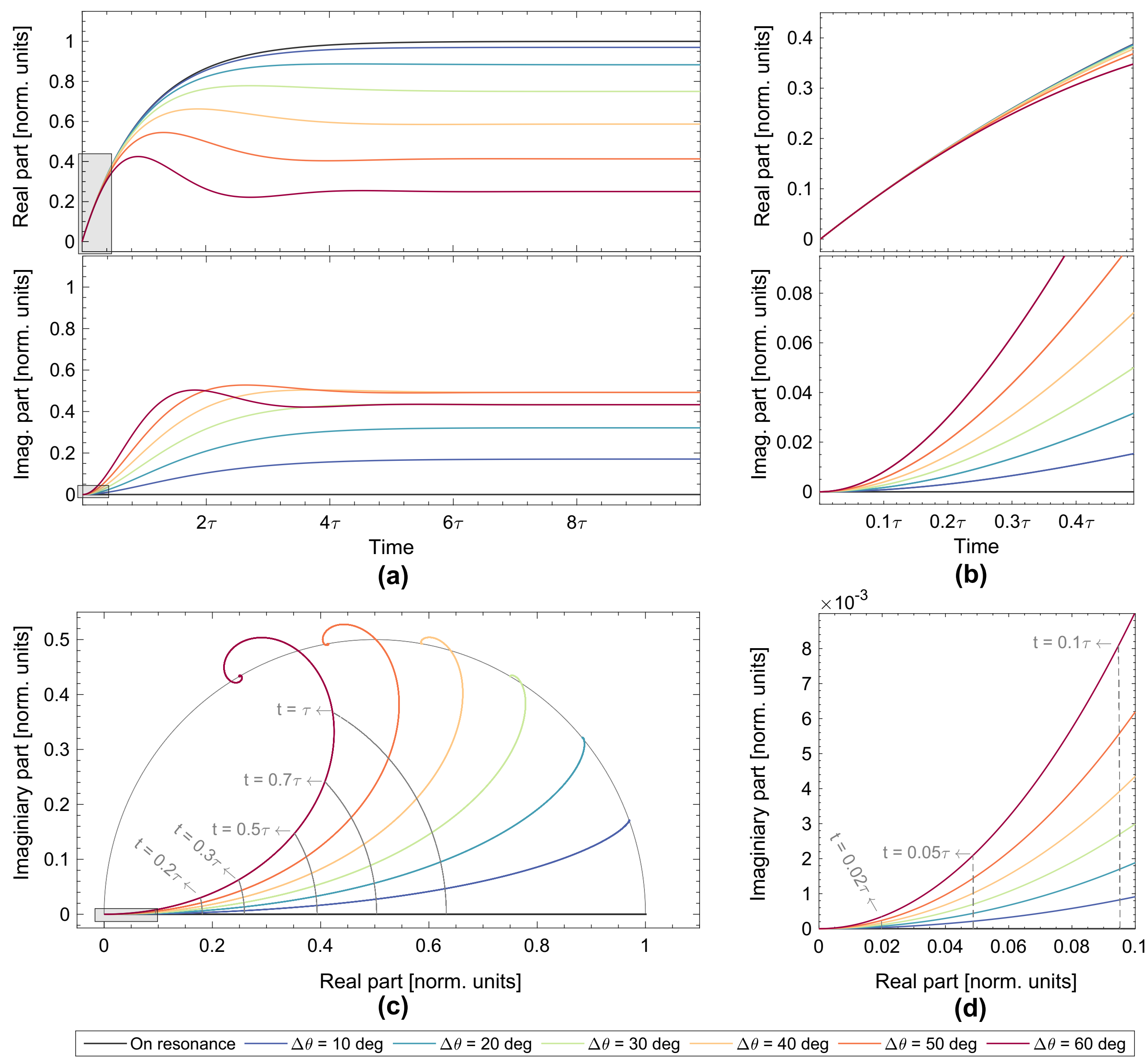


**Fig. 4** (Color online) Step response of Eq. (4) and the corresponding I/Q plane trajectories under different detuning angles $\Delta\theta$. **a** Simulated step response of $\mathbf{V}_{\mathrm{cb,step}}(t)$ for various $\Delta\theta$. The upper and lower subplots show the real and imaginary parts of the signals, respectively. **b** Zoom-in view of the gray-shaded region in subplot (a), highlighting the early-time behavior of the transient response. **c** I/Q plane trajectories of $\mathbf{V}_{\mathrm{cb,step}}(t)$ under different $\Delta\theta$. **d** Zoom-in view of the I/Q plane during the very early stage ($t < 0.02\tau$). In this regime, the trajectory of $\mathbf{V}_{\mathrm{cb,step}}(t)$ closely follows a straight line along the real axis. This effect is particularly pronounced when $\Delta\theta$ is small, where the imaginary component remains negligible compared to the real part

causing the corresponding transient vector to deviate from the direction of $\mathbf{V}_{\mathrm{b}}$ in the complex I/Q plane. The angle between $\mathbf{V}_{\mathrm{cb,step}}$ and $\mathbf{V}_{\mathrm{b}}$ is determined by both the detuning magnitude and observation time $t$. It is important to note that $t$ must remain less than the beam pulse width $T_{\mathrm{ps}}$ (see Fig. 2a), because the quasi-rectangular beam pulse can only be approximated as a step input within this interval.

For SC cavities, the loaded quality factor $Q_{\mathrm{L}}$ is typically high, resulting in a narrow half-bandwidth (tens to hundreds of Hz) and a large time constant $\tau$ on the order of milliseconds. Assuming $\tau = 3$ ms (as in the KEK cERL main linac cavity [17, 18]) and a beam pulse width of $T_{\mathrm{ps}} = 9$ µs, with a detuning angle of $\Delta\theta = 45°$, Eq. (9) yields $\mathfrak{I}[\mathbf{V}_{\mathrm{cb,step}}(t)]/\mathfrak{R}[\mathbf{V}_{\mathrm{cb,step}}(t)] \approx 0.0015$, corresponding to a phase deviation of arctan(0.0015) < 0.1°, which can be safely neglected.

In contrast, for the ESS NC buncher cavity B2 (see Fig. 1) with a time constant $\tau \approx 9$ μs, the same 9 μs beam pulse leads to a significantly different behavior. Even with a small detuning angle of $\Delta\theta = 5°$, the resulting deviation of $\mathbf{V}_{\rm cb}$ can exceed 5°, which is no longer negligible. As shown in the experimental results of Fig. 3, the buncher cavity B2 exhibits a detuning angle of approximately −11°. With a 5 μs beam pulse, this results in a slight deflection of the transient response $\mathbf{V}_{\rm cb}$ toward the negative direction of the X-axis in the I/Q plane.

It should be emphasized that Eq. (6) is valid only for the zero-state response of Eq. (4), where the beam-induced voltage $\mathbf{V}_{\rm b}(t)$ is modeled as a unit step function aligned along the X-axis. In practical measurements, however, the observed beam-induced RF transient also includes the steady-state cavity field, and the beam-induced voltage vector $\mathbf{V}_{\rm b}(t)$ may point in an arbitrary direction within the 360-degree I/Q plane. Therefore, the normalized transient signal $\mathbf{V}_{\rm cb}(t)$ is expressed as:

$$\mathbf{V}_{\rm cb}(t) = 1 + \frac{\omega_{0.5}\left[1 - e^{-(\omega_{0.5} - j\Delta\omega)t}\right]\mathbf{V}_{\rm b}}{(\omega_{0.5} - j\Delta\omega)V_{\rm c,ss}} \quad \text{for } 0 < t < T_{\rm ps} \tag{10}$$

where $V_{\rm c,ss}$ denotes the steady-state cavity voltage.

Substituting $\mathbf{V}_{\rm b}$ in Eq. (10) with $\mathbf{I}_{\rm b}$ using Eq. (2) yields:

$$\mathbf{V}_{\rm cb}(t) = 1 + \frac{\omega_{0.5}\left[1 - e^{-(\omega_{0.5} - j\Delta\omega)t}\right]\left(\frac{r}{Q}\right)Q_{\rm L}I_{\rm b0}e^{j\alpha}}{(\omega_{0.5} - j\Delta\omega)V_{\rm c,ss}} \quad \text{for } 0 < t < T_{\rm ps} \tag{11}$$

where $\alpha$ denotes the phase difference between the vectors $\mathbf{I}_{\rm b}$ and $\mathbf{V}_{\rm c}$. The beam phase $\varphi_{\rm b}$ is related to $\alpha$ by the expression $\varphi_{\rm b} = \pi - \alpha$, as shown in Fig. 2.

Figure 5 shows the simulation results based on Eq. (11), where different detuning angles produce distinct trajectories of $\mathbf{V}_{\rm cb}(t)$ in the I/Q plane. The simulation assumed a peak beam current of $I_{\rm b0} = 55$ mA, pulse width of 5 μs, and beam phase of approximately −45°. Figure 5a and b illustrate the time evolution of the amplitude and phase and the corresponding I/Q plane trajectories, respectively.

In this section, the beam excitation is approximated as a quasi-rectangular pulse with a submicrosecond rise time, as is typically observed in accelerator systems [22]. Based on this, the beam input was modeled as a unit step function to analyze the detuning effects on the beam phase measurement for both SC and NC cavities. Although this assumption simplifies the analysis, the qualitative conclusions remain valid for arbitrary beam pulse shapes. A general derivation is provided in Appendix A.

## 3 Beam phase calibration algorithm with detuning compensation

To enable accurate phase calibration under detuning, this section presents a correction framework based on a theoretical deflection estimation. We first derive the deflection angle induced by detuning and then discuss its application under closed-loop operation.

### 3.1 Theoretical estimation of deflection angle caused by detuning

According to Eq. (6) in Sect. II, the theoretical phase deflection angle $\alpha_{\rm th}$ induced by detuning $\Delta\omega$ at time $T_{\rm w}$ ($T_{\rm w}$ represents the calibration window for beam phase, $T_{\rm w} < T_{\rm ps}$) can be expressed as:

$$\alpha_{\rm th} = \arg\left(\mathbf{V}_{\rm cb}(t)\right)\big|_{t=T_{\rm w}}. \tag{12}$$

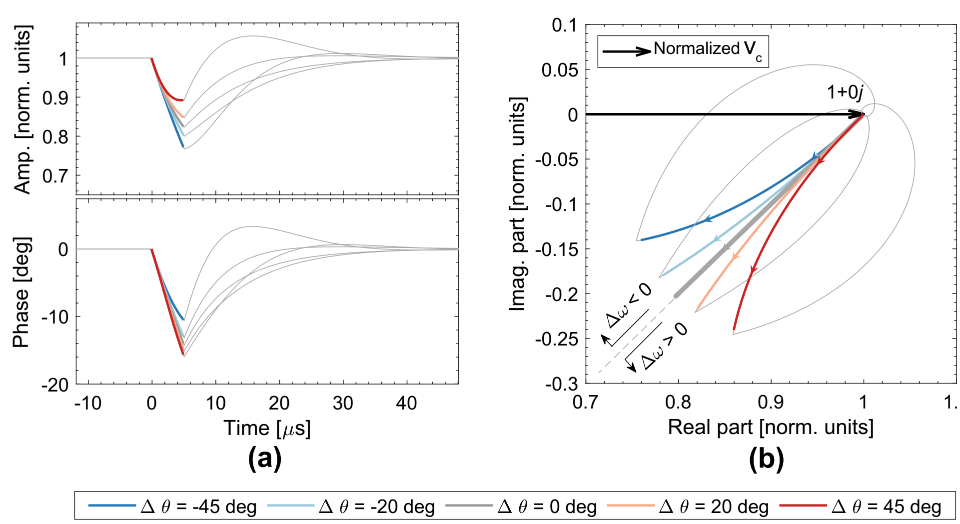


**Fig. 5** (Color online) Simulation results of beam-induced RF transient under various detuning angles $\Delta\theta$, assuming open-loop cavity operation ($I_{\rm b0} = 55$ mA, beam pulse width $T_{\rm ps} = 5$ μs, beam phase ≈ −45°). These parameter values were specified as the input conditions in the simulation model. **a** Time-domain waveforms of amplitude and phase under different $\Delta\theta$. **b** Corresponding trajectories of $\mathbf{V}_{\rm cb}$ in the I/Q plane

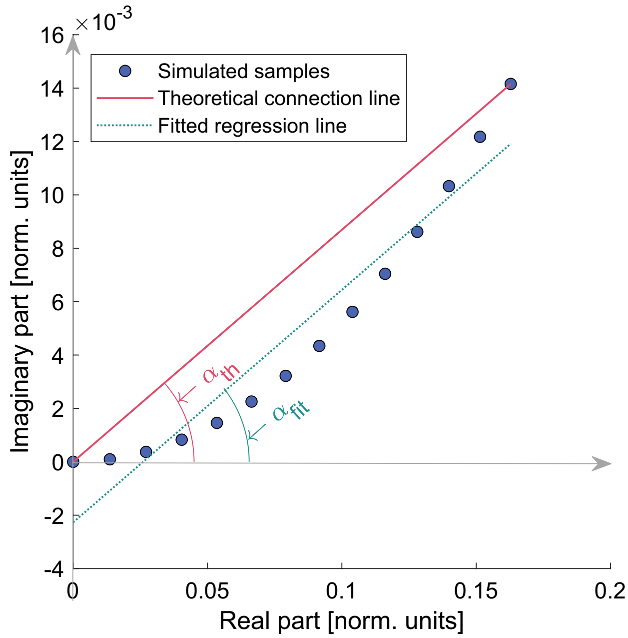


**Fig. 6** Comparison of the fitted deflection angle $\alpha_{fit}$ and the theoretical deflection angle $\alpha_{th}$ caused by cavity detuning. The blue dots represent the discretized I/Q plane trajectory of the step response $\mathbf{V}_{cb}(t)$, calculated from Eq. (6)

As shown in Fig. 6, the step response $\mathbf{V}_{cb}(t)$ in Eq. (6) is discretized as $t = nT_s$, where $T_s$ is the sampling period of the digital LLRF data acquisition system ($T_s \approx 0.119$ µs). Assuming that $\mathbf{V}_b$ points along the X-axis, the resulting discrete samples are plotted as blue dots in the I/Q plane. A linear regression of these points yields the green dashed line, with its angle relative to the X-axis denoted by $\alpha_{fit}$. The theoretical deflection angle $\alpha_{th}$, calculated from Eq. (12), corresponds to the angle between the X-axis and the line connecting the first and last sampled points. Because $\alpha_{th}$ reflects only the trajectory defined by the start and end points, whereas $\alpha_{fit}$ accounts for the overall sample distribution, the residual phase error $\Delta\alpha = \alpha_{fit} - \alpha_{th}$ is generally nonzero. In practical applications, $\alpha_{fit}$ is first extracted from the measured data and then corrected by subtracting $\alpha_{th}$ (see Sect. 3.2), making it necessary to evaluate whether the resulting $\Delta\alpha$ can be neglected in the analysis.

Figure 7 presents 2D contour plots of the theoretical deflection angle $\alpha_{th}$ (a) and the residual phase error $\Delta\alpha$ (b) as functions of the detuning angle $\Delta\theta$ and the observation time $T_w$, where $T_w \in [0, 0.5\tau]$ and $\Delta\theta \in [-45°, 45°]$. Although $\alpha_{th}$ and $\alpha_{fit}$ are derived differently, Fig. 7b shows that $\Delta\alpha$ remains negligibly small across the entire scan range. This confirms that in practical applications, when the fitting interval is limited to $0.5\tau$, the phasor $\mathbf{V}_b$ (or $\mathbf{I}_b$) can be accurately recovered by rotating the fitted trajectory by $-\alpha_{th}$. Because $\alpha_{th}$ can be directly calculated from Eq. (12), this method enables the effective compensation of detuning-induced phase errors in beam phase measurements.

### 3.2 Feasibility of closed-loop implementation

Having established the theoretical framework for detuning compensation, we now turn to its practical application under closed-loop conditions, which are essential for safe and stable beam delivery in high-current proton linacs, such as the ESS.

Accordingly, we exploit the LLRF loop delay window $\tau_d$, during which the cavity field responds only to the beam

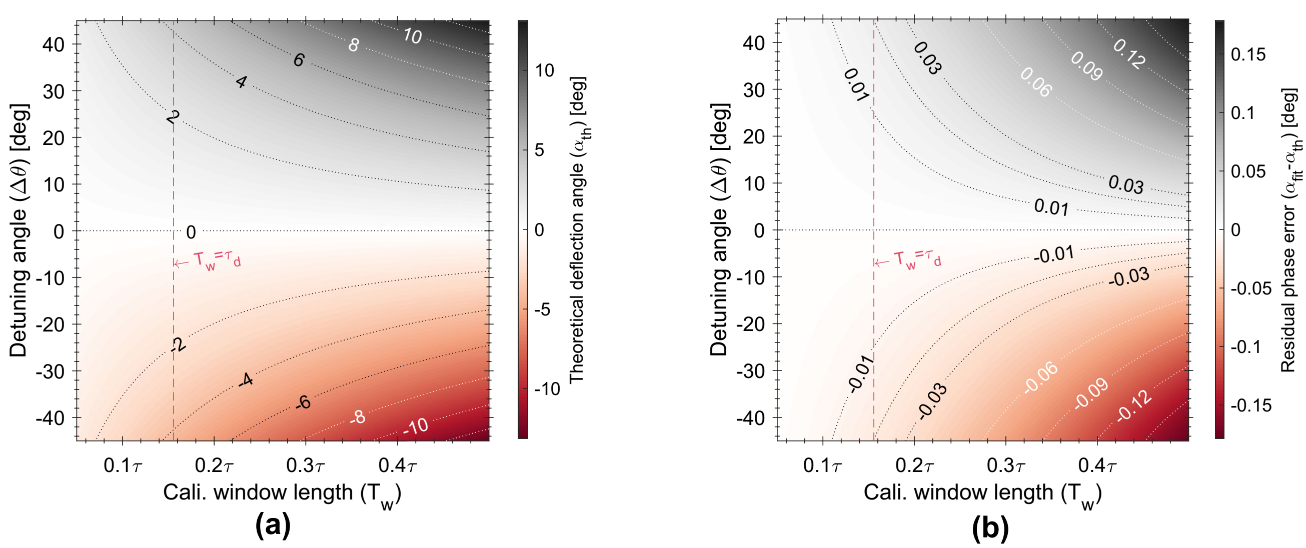


**Fig. 7** (Color online) Theoretical phase deflection angle $\alpha_{th}$ and residual phase error $\alpha_{fit} - \alpha_{th}$ versus detuning angle $\Delta\theta$ and calibration window $T_w$. **a** $\alpha_{th}$; **b** $\Delta\alpha = \alpha_{fit} - \alpha_{th}$, representing the difference between the two angles, as illustrated in Fig. 6. The dashed line indicates $T_w = \tau_d$

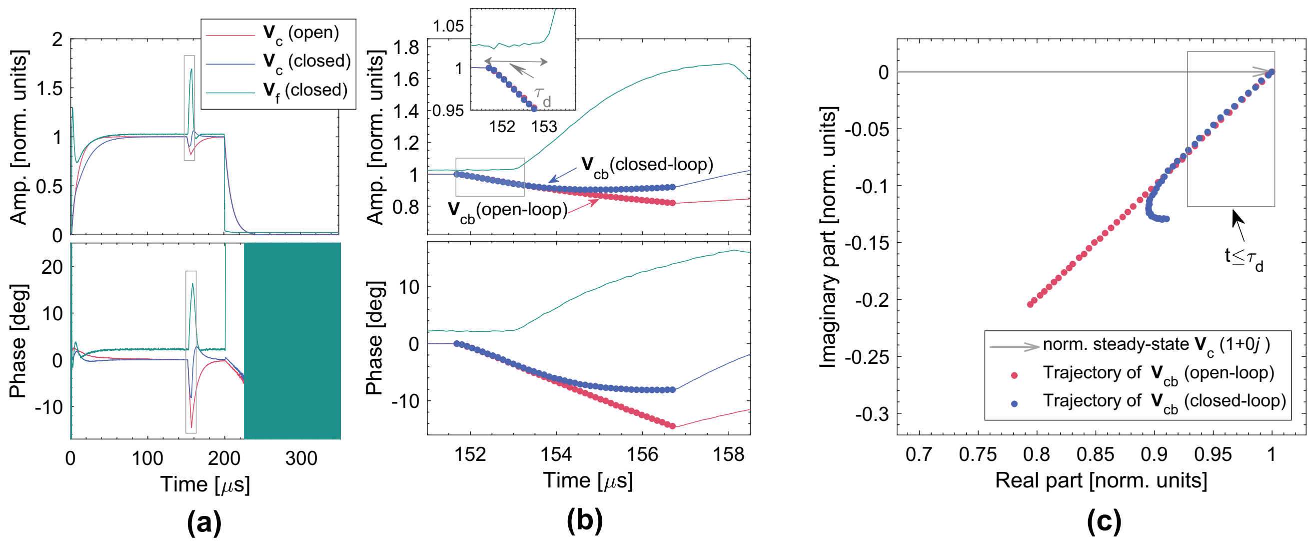


**Fig. 8** (Color online) Measured beam-induced RF transient in the ESS buncher cavity B2 under open- and closed-loop mode ($T_{ps}$=5 µs, $I_{b0}$=55 mA, $\varphi_b \approx -45°$). **a** Time evolution of the cavity voltage $\mathbf{V}_c$ for both modes and forward voltage $\mathbf{V}_f$ in the closed-loop mode. **b** Zoom-in view of the beam-induced RF transient. The beam arrives at approximately 151.6 µs, and the closed-loop system starts responding at around 153 µs due to a loop delay of $\tau_d \approx 1.4$ µs. During this delay window, the amplitude and phase of $\mathbf{V}_{cb}$ were nearly identical in both the open- and closed-loop cases. **c** Corresponding trajectories of $\mathbf{V}_{cb}$ in I/Q plane. The trajectories within the initial $\tau_d$ window show excellent agreement in the open- mode and closed-loop cases

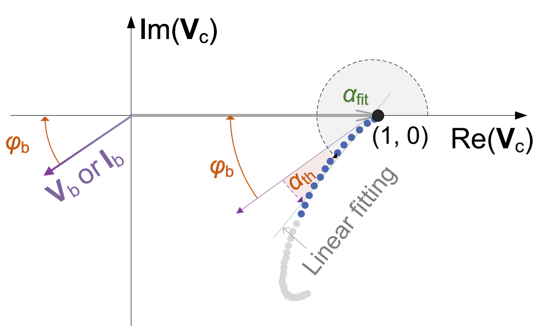


**Fig. 9** Beam phase calibration procedure in the closed-loop mode with cavity detuning. Blue dots show the trajectory of $\mathbf{V}_{cb}$ in the I/Q plane within the loop delay $\tau_d$; the green dashed line is the linear fit, giving $\alpha_{fit}$. After compensating for detuning-induced deflection $\alpha_{th}$, the beam phase is calculated via $\varphi_b = \pi - (\alpha_{fit} - \alpha_{th})$

and not to the feedback correction. As shown in Fig. 8a and Fig. 8b, the beam enters the cavity at approximately 151.6 µs, and the feedback system begins adjusting $\mathbf{V}_f$ at about 153 µs. Within this short interval ($\tau_d \approx 1.4$ µs), the system behaves equivalently to an open-loop operation, enabling an accurate measurement of the beam-induced transient. The close agreement between the open-loop and closed-loop trajectories in Fig. 8c demonstrates the feasibility of beam phase calibration in this mode.

Figure 9 illustrates the calibration process under closed-loop and detuned conditions. The beam phase $\varphi_b$ is calculated as follows:

1. Normalize the steady-state cavity voltage $\mathbf{V}_c$ prior to beam arrival to $1 + 0j$, which serves as the reference point in the I/Q plane.
2. Extract the transient response $\mathbf{V}_{cb}(t)$ within the loop delay window $\tau_d$, and perform linear fitting to obtain the fitted deflection angle $\alpha_{fit}$. Here, $\alpha_{fit}$ is extracted from the measured samples of $\mathbf{V}_{cb}$ at an arbitrary beam phase. For reference, Figs. 6 and 7 present $\alpha_{fit}$ obtained from the simulated samples for the special case in which the beam-induced vector is aligned with the X-axis. Because this case is physically equivalent to the general situation, we retain the same notation $\alpha_{fit}$ throughout this paper.
3. Compute the cavity detuning angle $\Delta\theta$ and corresponding frequency detuning $\Delta\omega$ at the beam arrival time (assuming detuning remains constant during the beam pulse):

$$\begin{cases} \Delta\theta = \angle\mathbf{V}_c - \angle\mathbf{V}_f \\ \Delta\omega = \tan(\Delta\theta) \cdot \omega_{0.5} \end{cases} \tag{13}$$

Here, $\mathbf{V}_c$ and $\mathbf{V}_f$ are the calibrated cavity and forward voltages, respectively, obtained by applying complex scaling factors derived from a linear regression calibration [24, 25]. Then, the theoretical deflection angle at $T_w = \tau_d$ is calculated using Eq. (12):
4. Finally, compute the beam phase using:

$$\varphi_b = \pi - (\alpha_{fit} - \alpha_{th}). \tag{14}$$

## 4 Experimental validation

The experimental validation of the detuning-compensated beam phase calibration algorithm, including its closed-loop feasibility, was conducted using the ESS MEBT normal-conducting buncher cavity (B2, Fig. 1). The beam pulse width was fixed at $T_{ps} = 5$ µs, with the beam current and phase adjusted as needed. BCTs and a BPM (in Q5, Fig. 1) independently measure the beam current and phase. RF pulse waveforms (Fig. 3, 8) and key RF parameters (Table 2) characterize the setup.

Figure 10 compares the measured beam-induced RF transients $\mathbf{V}_{cb}$ with the simulated results under various detuning angles $\Delta\theta$ in the open-loop mode. The measurements, shown as filled circles, aligned well with the simulated waveforms computed from Eq. (11), confirming the validity of the transient response model. With validated predictions, we evaluated the performance of the detuning compensation algorithm.

Figure 11 shows the open-loop beam phase measurements ($I_{b0} = 55$ mA) before and after the detuning correction. Subfigures (a) and (b) use $T_w = 1.4$ µs ($\tau_d$) and 3 µs. Individual (small markers) and average (larger filled circles/squares) measurements are shown. Applying the correction in Sect. 3.2 makes the measured beam phase insensitive to detuning, thereby confirming its effectiveness. Without correction, detuning angles of ±45° (corresponding to $\Delta\omega = \pm\omega_{0.5}$) result in phase errors of approximately 9° at $T_w = 1.4$ µs and 18° at $T_w = 3$ µs (approximately $0.34\tau$).

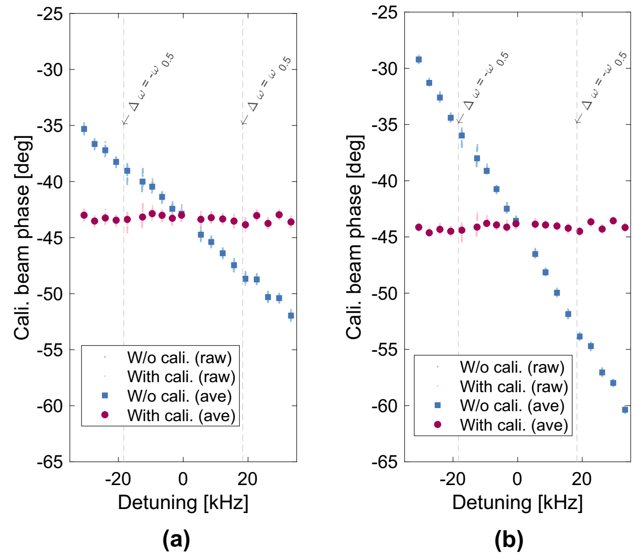


**Fig. 11** (Color online) Comparison of beam phase measurements before and after detuning correction under open-loop operation ($I_{b0} = 55$ mA). **a** and **b** correspond to the calibration window $T_w$ of approximately 1.4 µs ($\tau_d$) and 3 µs, respectively. Small markers represent individual measurement results, whereas larger filled circles and squares denote the averaged values over multiple measurements

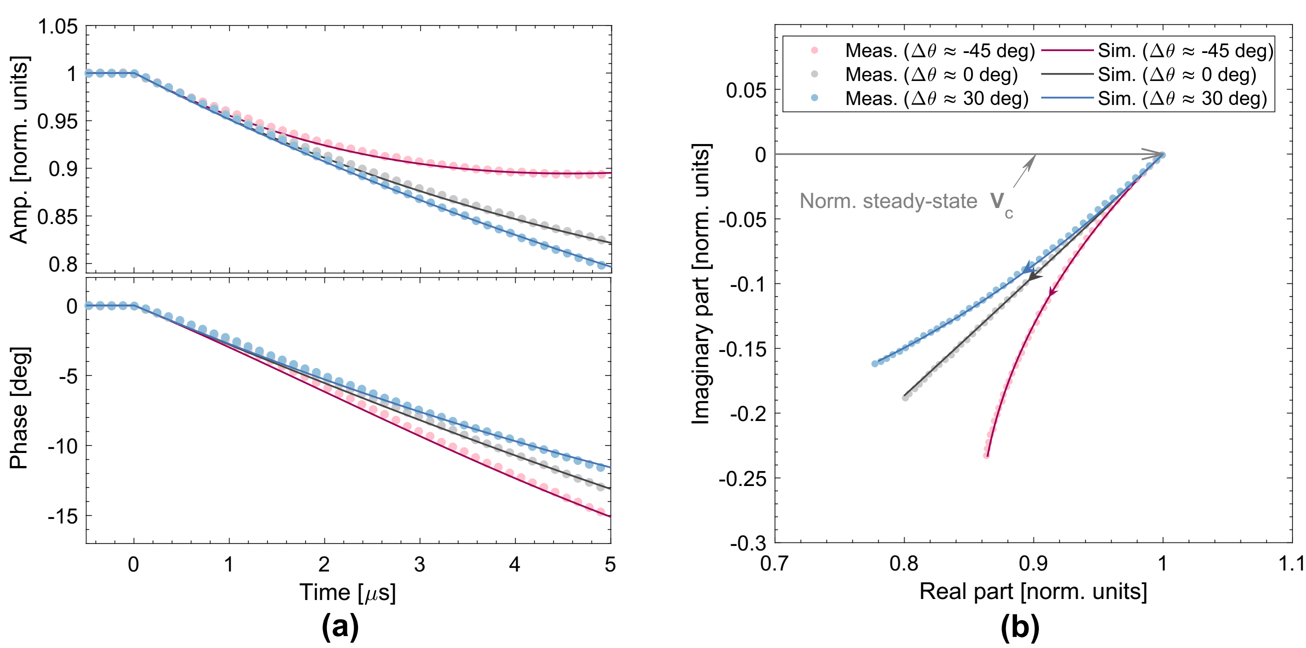


**Fig. 10** (Color online) Comparison of measured and simulated beam-induced RF transient $\mathbf{V}_{cb}$ in cavity B2 under open-loop operation for different detuning angles $\Delta\theta$. **a** Time-domain evolution of the amplitude and phase. **b** Corresponding trajectories of $\mathbf{V}_{cb}$ in the I/Q plane. The simulation curves (solid lines) were calculated using Eq. (11) and the experimental results are plotted as discrete dot markers

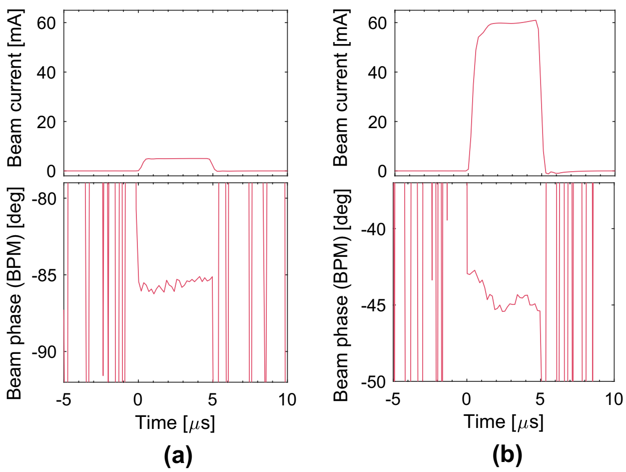


**Fig. 12** Measured beam current (top) and beam phase (bottom) using the BCT and BPM systems. Subfigures **a** and **b** correspond to beam currents $I_{b0} = 5$ mA and 60 mA, respectively

These results are consistent with the theoretical predictions shown in Fig. 7a.

To validate the method under realistic accelerator conditions, closed-loop beam phase measurements were conducted. Figure 12 shows the BCT and BPM measurements of the beam current (top) and phase (bottom). Figures 12a and b show low- ($I_{b0} = 5$ mA) and high-current ($I_{b0} = 60$ mA) cases. Notably, at a higher current, intrapulse phase fluctuations of approximately 2° are evident, and their impact on measurement precision is examined later.

Figure 13 compares the trajectories of the beam-induced transient signal $\mathbf{V}_{cb}$ in the I/Q plane under open-loop and closed-loop conditions. For the 5 mA case (Fig. 13a), the signal is relatively weak and more susceptible to noise, leading to reduced accuracy in phase determination. For the 60 mA case (Fig. 13 b), although the feedback introduces a slight curvature to the trajectory, the open-loop and closed-loop traces remain nearly identical within the loop delay window (approximately 13 samples, including the initial $1 + 0j$ sampling point), confirming the closed-loop feasibility.

The impact of the calibration window length $T_w$ was further evaluated for 5 mA and 60 mA beam currents in the open- and closed-loop modes. Figure 14 summarizes the results. Figure 14a and b show probability density histograms of the measured beam phase for various $T_w$, with upper plots for open-loop and lower for closed-loop. Different colors represent different $T_w$.

At 5 mA (Fig. 14a), under open-loop operation, increasing the calibration window $T_w$ leads to a narrower beam phase distribution, corresponding to a lower root-mean-square (RMS) error. The histogram peak stabilizes at approximately −85.5°, which is consistent with the theoretical prediction shown in Fig. 12a. After switching to the closed-loop operation, the measurements remained in good agreement with the open-loop results when $T_w \leq \tau_d$. However, deviations appear for $T_w > \tau_d$ because the feedback response begins to affect $\mathbf{V}_{cb}$ (see Fig. 8c).

At 60 mA (Fig. 14b), under open-loop operation, the phase distributions are more concentrated due to improved signal-to-noise ratio. Nevertheless, intrapulse beam phase fluctuations (as observed in Fig. 12b) cause the histogram

**Fig. 13** (Color online) Trajectories of the beam-induced RF transient $\mathbf{V}_{cb}$ in the I/Q plane under open-loop (red) and closed-loop (blue) operations. **a** $I_{b0} = 5$ mA, **b** $I_{b0} = 60$ mA. The four trajectories in each subplot correspond approximately to beam phases of 1°, −18°, −44°, and −89°

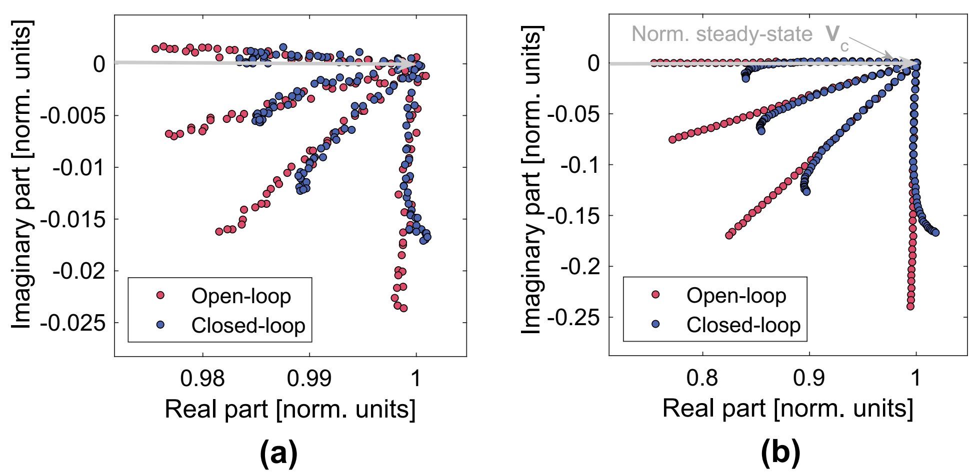

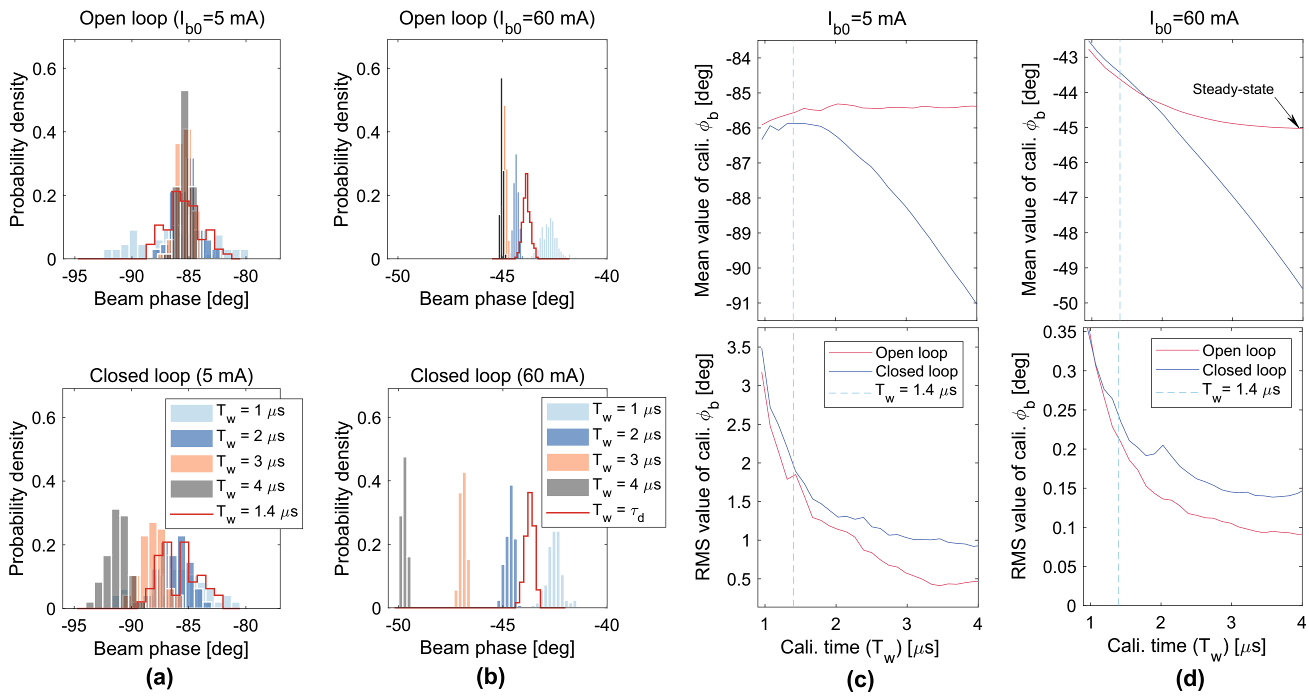


**Fig. 14** (Color online) **a**, **b** Histograms of beam phase measurements obtained under different calibration window lengths $T_w$, for open-loop and closed-loop operations, respectively. The beam current and phase settings used in **a** and **b** correspond to those shown in Fig. 12a and Fig. 12b. **c**, **d** Mean values (top) and RMS errors (bottom) of beam phase measurements versus calibration window $T_w$. In **d**, under open-loop operation with $I_{b0} = 60$ mA, the mean value results suggest that the beam phase reaches steady state at approximately 3.5 μs. The vertical dashed lines indicate the results obtained at the loop delay $\tau_d = 1.4$ μs

peak to shift with increasing $T_w$, for example, from approximately $-42.5°$ at $T_w = 1$ $\mu$s to $-45°$ at $T_w = 4$ $\mu$s. Under closed-loop operation, a similar trend is observed: the results match the open-loop reference when $T_w \le \tau_d$, but deviate for $T_w > \tau_d$ as the feedback response begins to affect $\mathbf{V}_{cb}$.

Figures 14c and 14d present the average (top) and RMS error (bottom) of the measured beam phase versus $T_w$ for the 5 mA and 60 mA cases. For 5 mA (Fig. 14c), the average phase remains stable across different $T_w$ under open-loop conditions. Under closed-loop operation, it matches the open-loop reference when $T_w \le \tau_d$, but deviates for larger $T_w$. The RMS error decreased monotonically with increasing $T_w$, indicating that a larger calibration window improved the robustness of the phase measurement. For 60 mA (Fig. 14d), although the overall measurement precision is higher, intrapulse phase fluctuations still introduce deviations in both open- and closed-loop results, as previously discussed.

Figure 15 compares the calibrated beam phase (blue), obtained from $\mathbf{V}_{cb}$ fit under closed-loop operation, with BPM5 measurements (green) across different beam currents. The BPM data are obtained by averaging the phase signal over the 2.5–5 μs interval (see Fig. 12). BPM measurements revealed beam phase differences at various currents. This may be attributed to the defocusing effects of the buncher

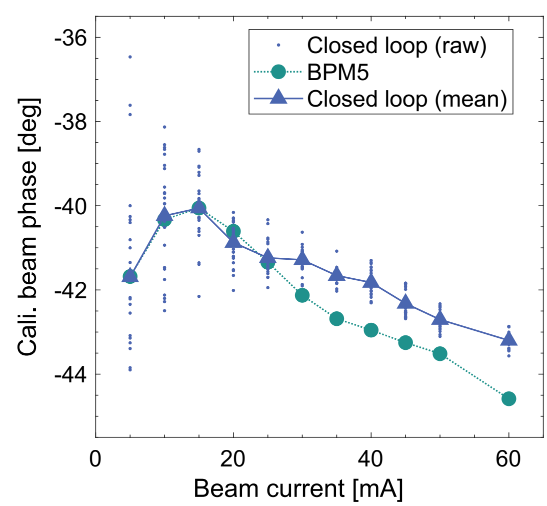


**Fig. 15** (Color online) Comparison of the calibrated beam phase (blue) and BPM measurements (green). Small dots represent individual measurements, and larger markers indicate the average over multiple shots. The BPM phase values are calculated by averaging the beam phase signal over the 2.5–5 μs interval (see Fig. 12)

cavity, where beams of different intensities pass through the cavity along slightly different orbits, thereby causing variations in the BPM readings. As shown in Fig. 15, at low

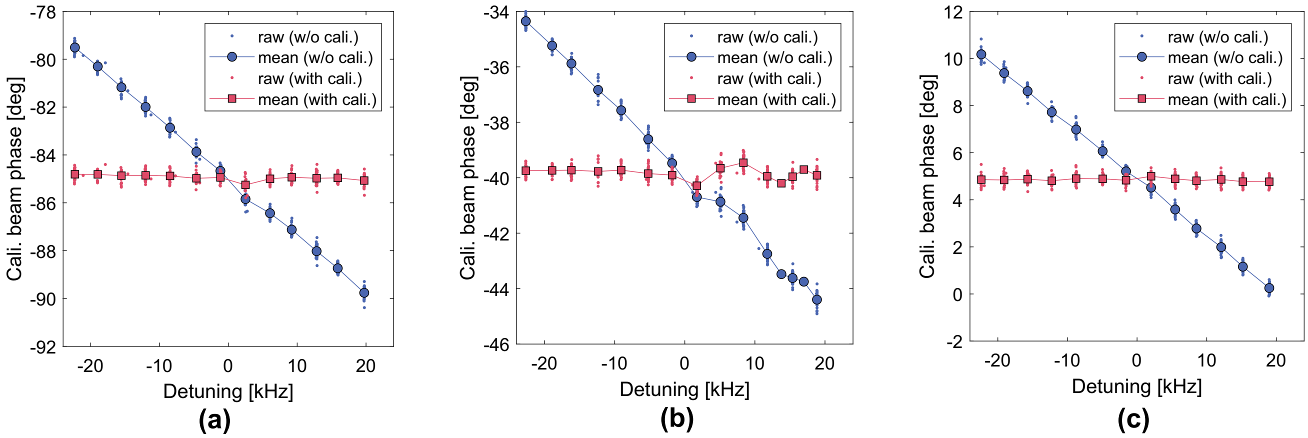


**Fig. 16** (Color online) Comparison of beam phase measurements under closed-loop operation before and after detuning compensation at a beam current of $I_{b0} = 60$ mA. Subfigures **a**, **b**, and **c** correspond to different beam phase settings. Small dots represent individual measurements, whereas larger solid markers (circles and squares) denote the averaged results before and after correction, respectively

beam currents, BPM5 measurements match well with the calibrated beam phase from the $\mathbf{V}_{cb}$ fit under closed-loop operation. However, at higher currents, increasing deviations (approximately 1.5°) are observed owing to beam phase fluctuations during the pulse duration (see Fig. 12b). It should be noted that BPM-based measurements are generally considered more accurate because they average the beam phase over the entire pulse, particularly during the steady-state portion. In this study, a dedicated phase-scan calibration was carefully performed a few days prior to the experiment, which minimized the impact of possible ambient drifts on the BPM results.

Figure 16 presents the closed-loop beam phase measurement results with a calibration window of $T_w = \tau_d$, at a beam current of $I_{b0} = 60$ mA. Subfigures (a), (b), and (c) correspond to the different beam phase settings. Before calibration (blue), the measured beam phase exhibited a clear linear dependence on the cavity detuning. After applying the correction method described in Sect. III.B (red), this dependence was effectively eliminated, and the beam phase remained stable across the full detuning range. These results provide strong experimental validation for the proposed detuning compensation algorithm.

In summary, the experimental data validate the effectiveness of the proposed method in compensating for detuning effects and achieving accurate beam phase measurements under realistic accelerator conditions. This approach enables noninvasive, online beam phase calibration under fully closed-loop operation, even in high-current normal-conducting cavities, such as those at the ESS. By avoiding disruption of routine operations, this method provides a practical and scalable solution for real-time diagnostics, routine calibration, and early fault detection in modern proton linacs [23].

## 5 Conclusions and future work

In this study, we systematically investigated a beam phase measurement method based on transient beam loading and quantitatively analyzed the influence of cavity detuning on the measurement results for both superconducting and normal-conducting RF cavities. A theoretical expression for the detuning-induced phase deflection angle was derived, and a compensation algorithm was proposed. The feasibility of implementing this method was experimentally validated using the buncher cavity (B2) in the MEBT section of the ESS accelerator. The effectiveness of the proposed algorithm was demonstrated by comparing the open-loop and closed-loop measurements under various detuning scenarios.

The results confirm that within the LLRF loop delay window ($\tau_d$), the transient vector $\mathbf{V}_{cb}$ evolves similarly under both open- and closed-loop modes, thereby enabling a reliable beam phase determination. Nonetheless, the limited length of $\tau_d$ restricts the number of samples available for fitting, and low-current conditions reduce the phase resolution owing to the lower signal-to-noise ratios. Under higher beam currents, intrapulse phase fluctuations introduce systematic offsets compared with BPM-based measurements. Despite these limitations, closed-loop calibration offers enhanced operational stability and is better suited for continuous beam phase monitoring in linacs.

When both detuning and feedback are present, the trajectory of $\mathbf{V}_{cb}$ in the I/Q plane becomes more complex, but still follows identifiable patterns. Future research may leverage artificial intelligence (AI) techniques to overcome the current $T_w \leq \tau_d$ limitation, thereby enabling accurate phase recovery even beyond the initial transient regime.

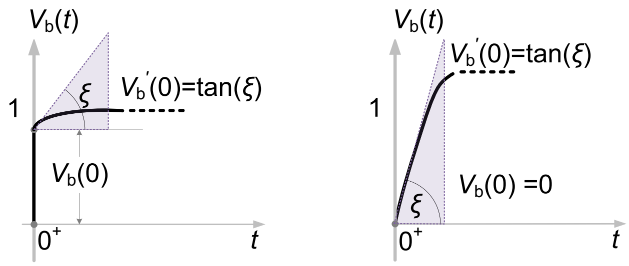


**Fig. 17** Typical shapes of the $V_b(t)$ as $t \to 0^+$: left: $V_b(0) \neq 0$; right: $V_b(0) = 0$

Preliminary investigations in this direction have shown promising results [16].

## Appendix A: early-time expansion of the cavity response

To analyze the early-time behavior of the cavity response under beam-induced excitation, consider the following first-order differential equation:

$$\frac{d\mathbf{V}_{cb}}{dt} + \lambda \mathbf{V}_{cb}(t) = \omega_{0.5} V_b(t), \quad \mathbf{V}_{cb}(0) = 0, \tag{A.1}$$

where $\lambda = \omega_{0.5} - j\Delta\omega$, and $V_b(t)$ is an arbitrary causal input with $V_b(t < 0) = 0$.

We focus on the limit $t \to 0^+$, immediately after the beam pulse begins. Figure 17 illustrates the typical shapes of $V_b(t)$ as $t \to 0^+$, distinguishing between the cases $V_b(0) \neq 0$ and $V_b(0) = 0$. To simplify the analysis without loss of generality, we assumed that the beam phase remained constant within the pulse duration and set the initial beam phase to zero. Thus, $V_b(t) \in \mathbb{R}^+$.

The system's zero-state solution is:

$$\mathbf{V}_{cb}(t) = \omega_{0.5} \int_0^t e^{-\lambda(t-x)} V_b(x)\, dx. \tag{A.2}$$

Expand $V_b(x)$ near $x = 0$:

$$V_b(x) = V_b(0) + V_b'(0)\, x + \mathcal{O}(x^2). \tag{A.3}$$

Substitute Eq. (A.3) into Eq. (A.2), and change variables via $s = t - x$, we obtain:

$$\mathbf{V}_{cb}(t) \approx \omega_{0.5} \int_0^t e^{-\lambda s} \left[ V_b(0) + V_b'(0)(t - s) \right] ds. \tag{A.4}$$

Using $e^{-\lambda s} \approx 1 - \lambda s$ as $s \to 0$, the integral becomes:

$$\mathbf{V}_{cb}(t) \approx \omega_{0.5} \Big[ V_b(0) \int_0^t (1 - \lambda s)\, ds + V_b'(0) \int_0^t (t - s)(1 - \lambda s)\, ds \Big]. \tag{A.5}$$

$$\int_0^t (1 - \lambda s)\, ds = t - \frac{1}{2}\lambda t^2, \tag{A.6}$$

$$\int_0^t (t - s)(1 - \lambda s)\, ds = \frac{1}{2}t^2 - \frac{1}{6}\lambda t^3. \tag{A.7}$$

Substituting Eqs. (A.6)–(A.7) into Eq. (A.5), the response becomes:

$$\mathbf{V}_{cb}(t) \approx \omega_{0.5} \Big[ V_b(0)\Big(t - \frac{1}{2}\lambda t^2\Big) + V_b'(0)\Big(\frac{1}{2}t^2 - \frac{1}{6}\lambda t^3\Big) \Big]. \tag{A.8}$$

$$\Re[\mathbf{V}_{cb}(t)] \approx \omega_{0.5} \Big[ V_b(0)\Big(t - \frac{1}{2}\omega_{0.5} t^2\Big) + V_b'(0)\Big(\frac{1}{2}t^2 - \frac{1}{6}\omega_{0.5} t^3\Big) \Big], \tag{A.9}$$

$$\Im[\mathbf{V}_{cb}(t)] \approx \omega_{0.5} \Big[ \frac{1}{2}\Delta\omega V_b(0) t^2 + \frac{1}{6}\Delta\omega V_b'(0) t^3 \Big]. \tag{A.10}$$

$$\frac{\Im[\mathbf{V}_{cb}(t)]}{\Re[\mathbf{V}_{cb}(t)]} \approx \begin{cases} \dfrac{\frac{1}{2}\Delta\omega t + \frac{1}{6}\Delta\omega \frac{V_b'(0)}{V_b(0)} t^2}{1 - \frac{1}{2}\omega_{0.5} t + \frac{1}{2}\frac{V_b'(0)}{V_b(0)} t} + \mathcal{O}(t^2), & \text{if } V_b(0) \neq 0, \\ \dfrac{\frac{1}{3}\Delta\omega t}{1 - \frac{1}{3}\omega_{0.5} t} + \mathcal{O}(t^2), & \text{if } V_b(0) = 0. \end{cases} \tag{A.11}$$

For a unit step input $V_b(t) = u(t)$, we have $V_b(0) = 1$ and $V_b'(0) = 0$. Substituting into Eq. (A.11):

$$\frac{\Im[\mathbf{V}_{cb}(t)]}{\Re[\mathbf{V}_{cb}(t)]} \approx \frac{\frac{1}{2}\Delta\omega t}{1 - \frac{1}{2}\omega_{0.5} t} + \mathcal{O}(t^2). \tag{A.12}$$

Finally, the limit of the imaginary-to-real ratio is

$$\lim_{t \to 0^+} \frac{\Im[\mathbf{V}_{cb}(t)]}{\Re[\mathbf{V}_{cb}(t)]} = 0. \tag{A.13}$$

This result can be interpreted as follows. At an early stage, the cavity response vector aligns with the initial phase of the input signal. The detuning term $\Delta\omega$ contributes only to higher-order terms and does not cause an immediate phase rotation. Although the derivation assumes a constant beam phase, the result still holds if the phase varies smoothly near

$t = 0$, as such variations affect only higher-order corrections. A detailed treatment of the time-varying phase is beyond the scope of this appendix.

**Author contributions** All authors contributed to the study conception and design. Material preparation, data collection and analysis were performed by Feng Qiu, Ri-Hua Zeng and Cheng-Ye Xu. The first draft of the manuscript was written by Feng Qiu and all authors commented on previous versions of the manuscript. All authors read and approved the final manuscript.

**Data availability** The data that support the findings of this study are openly available in Science Data Bank at https://cstr.cn/31253.11.sciencedb.j00186.00955 and https://www.doi.org/10.57760/sciencedb.j00186.00955.

## Declarations

**Conflict of interest** Yuan He is an editorial board member for Nuclear Science and Techniques and was not involved in the editorial review, or the decision to publish this article. All authors declare that there are no conflict of interest.

## References


1. R. Garoby, A. Vergara, H. Danared et al., The European spallation source design. Phys. Scr. **93**, 014001 (2018). https://doi.org/10.1088/1402-4896/aa9bff
2. R. Miyamoto, C. Amstutz, S. Armanet et al., Beam commissioning of normal conducting part and status of ESS project, In: Proceedings of the 31st Linear Accelerator Conference (LINAC2022), Liverpool, UK, 28 August–2 September 2022. https://doi.org/10.18429/JACoW-LINAC2022-MO1PA02
3. Y. Levinsen, R. Miyamoto, N. Milas, et al., ESS normal conducting linac commissioning results. In: Proceedings of the 68th Advanced Beam Dynamics Workshop on High-Intensity High-Brightness Hadron Beams (HB2023), Geneva, Switzerland, 5–9 June 2023. https://doi.org/10.18429/JACoW-HB2023-TUA3I3
4. Y. Levinsen, M. Akhyani, R. Baron et al., First RF phase scans at the European Spallation Source. In: Proceedings of the 11th International Beam Instrumentation Conference (IBIC2022), Kraków, Poland, 11–15 September 2022. https://doi.org/10.18429/JACoW-IBIC2022-TUP35
5. A. Feschenko, S. Bragin, Y. Kiselev et al., Development and implementation of $\delta t$ procedure for the SNS linac. In: Proceedings of the 2005 Particle Accelerator Conference (PAC05), Knoxville, Tennessee, USA, 2005, pp. 3064–3066. https://doi.org/10.1109/PAC.2005.1591365
6. K. Crandall, The AT tune-up procedure for the LAMPF 805-MHz linac, Los Alamos Laboratory Report LA-6374-MS, 1976. Available at https://www.osti.gov/servlets/purl/7353211
7. R. Zeng, O. Troeng, Transient beam loading based calibration for cavity phase and amplitude setting. In: Proceedings of the 57th ICFA Advanced Beam Dynamics Workshop on High-Intensity and High-Brightness Hadron Beams (HB2016), Malmö, Sweden, 2016. Available at https://accelconf.web.cern.ch/hb2016/papers/mopl025.pdf
8. J. Galambos, A. Aleksandrov, C. Deibele, et al., Pasta-an RF phase scan and tuning application. In: Proceedings of the 2005 Particle Accelerator Conference, Knoxville, Tennessee, USA, 2005, pp. 1491–1493. https://doi.org/10.1109/PAC.2005.1590810
9. Y. Zhang, I. Campisi, P. Chu et al., Determination of field amplitude and synchronous phase using the beam-induced signal in an unpowered superconducting cavity. Nucl. Instrum. Methods Phys. Res. A **571**, 574–582 (2007). https://doi.org/10.1016/j.nima.2006.10.397
10. S.N. Simrock, T. Schilcher, DESY, Transient beam loading based calibration of the vector-sum for the TESLA test facility. In: Proceedings of the 8th Workshop on RF Superconductivity, Abano Terme, Italy, 1997, pp. 786–790. https://accelconf.web.cern.ch/e96/PAPERS/THPL/THP025L.PDF
11. P. Pawlik, M. Grecki, S. Simrock et al., New method for beam induced transient measurement. Meas. Sci. Technol. **18**, 2348–2355 (2007). https://doi.org/10.1088/0957-0233/18/8/008
12. M. Grecki, V. Ayvazyan, J. Branlard et al., On-line RF amplitude and phase calibration. In: Proceedings of the 8th International Particle Accelerator Conference (IPAC2017), Copenhagen, Denmark, 2017, pp. 3957–3960. https://doi.org/10.18429/JACoW-IPAC2017-THPAB103
13. N. Walker, Experience with beam-transient LLRF calibration in XFEL. In: Oral presentation of DESY-TEMF Collaboration Meeting, 11 Feb., 2020. Available at https://www.temf.tu-darmstadt.de/media/temf_emft/pdfs/desy/2020-11-02_Nick_Walker_Calibration.pdf
14. N. Walker, V. Ayvazyan, J. Branlard et al., Beam-transient-based LLRF voltage signal calibration for the European XFEL. In: Proceedings of 31st Linear Accelerator Conference (LINAC22), Liverpool, UK, 28 August–2 September 2022. https://doi.org/10.18429/JACoW-LINAC2022-MOPOPA03
15. F. Qiu, On-line beam synchronous phase calibration using beam-induced RF signals. In: Invited oral presentation of the 13th International Beam Instrumentation Conference (IBIC2024), Beijing, China, 9–13 September 2024. https://indico.jacow.org/event/80/contributions/5837/
16. L.J. Yang, On-line beam phase and current measurement using deep learning models. In: Oral presentation of the 2024 LLRF Topical Workshop – Timing, Synchronization, Measurements and Calibration (LLRF2024), Rome, Italy, 28–30 October 2024. Available at: https://agenda.infn.it/event/42239/contributions/244839/
17. F. Qiu, T. Miura, D. Arakawa et al., Application of disturbance observer-based control on pulsed superconducting radio frequency cavities. Phys. Rev. Accel. Beams **24**, 012804 (2021). https://doi.org/10.1103/PhysRevAccelBeams.24.012804
18. F. Qiu, T. Miura, D. Arakawa et al., RF commissioning of the compact energy recovery linac superconducting cavities in pulse mode. Nucl. Instrum. Methods Phys. Res. A **985**, 164660 (2021). https://doi.org/10.1016/j.nima.2020.164660
19. P. Sha, W. Pan, S. Jin et al., Ultrahigh accelerating gradient and quality factor of CEPC 650 MHz superconducting radio-frequency cavity. Nucl. Sci. Tech. **33**, 125 (2022). https://doi.org/10.1007/s41365-022-01109-8
20. J.Y. Ma, C.Y. Xu, A.D. Wu et al., Measurement of the cavity-loaded quality factor in superconducting radio-frequency systems with mismatched source impedance. Nucl. Sci. Tech. **34**, 123 (2023). https://doi.org/10.1007/s41365-023-01281-5
21. L.J. Yang, J.Y. Peng, F. Qiu et al., Classification of superconducting radio-frequency cavity faults of CAFE2 using machine learning. Nucl. Sci. Tech. **36**, 104 (2025). https://doi.org/10.1007/s41365-025-01685-5
22. C. Xu, Z. Zhu, F. Qiu et al., Application of a modified iterative learning control algorithm for superconducting radio-frequency cavities. Nucl. Instrum. Methods Phys. Res. A **1026**, 166237 (2022). https://doi.org/10.1016/j.nima.2021.166237
23. R. Zeng, Approach to calibrate beam phase using steady-state RF forward signal under closed-loop operation. In: Oral presentation at the 11th Low-Level Radio Frequency Workshop (LLRF2023),

Gyeongju, Republic of Korea, 22–27 October 2023. https://www.indico.kr/event/29/contributions/374/
24. F. Qiu, Y. He, A.-D. Wu et al., In situ mitigation strategies for field emission-induced cavity faults using low-level radiofrequency system. Nucl. Sci. Tech. **33**, 140 (2022). https://doi.org/10.1007/s41365-022-01125-8
25. J.Y. Ma, L.J. Yang, F. Qiu et al., Virtual cavity probe for the real-time identification of cavity burst-noise type in superconducting radio-frequency systems. Nucl. Instrum. Methods Phys. Res. A **1068**, 169786 (2024). https://doi.org/10.1016/j.nima.2024.169786
26. T. Schilcher, Vector sum control of pulsed accelerating fields in Lorentz force detuned superconducting cavities. Ph.D. thesis, University of Hamburg, 1998.https://bib-pubdb1.desy.de/record/291638/files/
27. A. Brandt, Development of a finite state machine for the automated operation of the LLRF control at FLASH, Ph.D. thesis, University of Hamburg, 2007. https://www.osti.gov/etdeweb/biblio/20930559
28. F. Qiu, S. Michizono, T. Miura et al., Real-time cavity simulator-based low-level radio-frequency test bench and applications for accelerators. Phys. Rev. Accel. Beams **21**, 032003 (2018). https://doi.org/10.1103/PhysRevAccelBeams.21.032003
29. F. Qiu, J.Y. Ma, G.D. Jiang et al., Approach to calibrate actual cavity forward and reflected signals for continuous wave-operated cavities. Nucl. Instrum. Methods Phys. Res. A **1034**, 166769 (2022). https://doi.org/10.1016/j.nima.2022.166769
30. R. Huang, Y. He, A phenomenological model of the fundamental power coupler for a superconducting resonator. Nucl. Sci. Tech. **34**, 167 (2023). https://doi.org/10.1007/s41365-023-01215-1